Development of a Symmetric Echo-Planar Spectroscopy Imaging Framework for Hyperpolarized 13C Imaging in a Clinical PET/MR Scanner

Eldirdiri, Abubakr; Posse, Stefan; Hanson, Lars G. ; Hansen, Rie Beck; Holst, Pernille; Schøier, Christina; Kristensen, Annemarie T; Johannesen, Helle Hjorth; Kjær, Andreas ; Hansen, Adam E

Total number of authors:
11

Published in:
Tomography - A Journal for Imaging Research

Link to article, DOI:
10.18383/j.tom.2018.00006

Publication date:
2018

Document Version
Publisher's PDF, also known as Version of record

TOMOGRAPHY® RESEARCH ARTICLE

Development of a Symmetric Echo-Planar Spectroscopy Imaging Framework for Hyperpolarized ^{13}C Imaging in a Clinical PET/MR Scanner

Abubakr Eldirdiri[1,2], Stefan Posse[3,4,5], Lars G. Hanson[1,2], Rie B. Hansen[1], Pernille Holst[7], Christina Schøier[7], Annemarie T Kristensen[7], Helle Hjorth Johannesen[6], Andreas Kjaer[6], Adam E. Hansen[6], and Jan Henrik Ardenkjaer-Larsen[1]

[1]Department of Electrical Engineering, Center for Hyperpolarization in Magnetic Resonance, Technical University of Denmark, Denmark; [2]Danish Research Centre for Magnetic Resonance, Centre for Functional and Diagnostic Imaging and Research, Copenhagen University Hospital Hvidovre, Denmark; Departments of [3]Neurology, [4]Physics and Astronomy, [5]Electrical and Computer Engineering, University of New Mexico, Albuquerque, NM, [6]Department of Clinical Physiology, Nuclear Medicine & PET and Cluster for Molecular Imaging, Rigshospitalet, University of Copenhagen, Copenhagen, Denmark; [7]Department of Veterinary Clinical Sciences, Faculty of Health and Medical Sciences, University of Copenhagen, Frederiksberg C, Denmark

Corresponding Author:
Jan Henrik Ardenkjaer-Larsen, PhD
Department of Electrical Engineering, Technical University of Denmark,
2800 Kgs Lyngby, Denmark;
E-mail: jhar@elektro.dtu.dk

Key Words: hyperpolarization, echo-planar spectroscopic imaging, regridding, metabolic imaging, cancer, molecular imaging, PET/MRI, hyperPET

Abbreviations: Echo-planar spectroscopic imaging (EPSI), chemical-shift imaging (CSI), positron emission tomography (PET), magnetic resonance imaging (MRI), multiecho balanced steady-state free precession (ME-bSSFP), magnetic resonance spectroscopy imaging (MRSI), spectral bandwidth (SW), magnetic resonance (MR), signal-to-noise ratio (SNR), fast Fourier transform (FFT), free induction decay (FID), analog-to-digital converter (ADC), repetition time (TR), echo time (TE), spin echo (SE), field of view (FOV)

ABSTRACT

Here, we developed a symmetric echo-planar spectroscopic imaging (EPSI) sequence for hyperpolarized ^{13}C imaging on a clinical hybrid positron emission tomography/magnetic resonance imaging system. The pulse sequence uses parallel reconstruction pipelines to separately reconstruct data from odd-and-even gradient echoes to reduce artifacts from gradient imbalances. The ramp-sampled data in the spatiotemporal frequency space are regridded to compensate for the chemical-shift displacements. Unaliasing of nonoverlapping peaks outside of the sampled spectral width was performed to double the effective spectral width. The sequence was compared with conventional phase-encoded chemical-shift imaging (CSI) in phantoms, and it was evaluated in a canine cancer patient with ameloblastoma after injection of hyperpolarized [1-^{13}C]pyruvate. The relative signal-to-noise ratio of EPSI with respect to CSI was 0.88, which is consistent with the decrease in sampling efficiency due to ramp sampling. Data regridding in the spatiotemporal frequency space significantly reduced spatial blurring compared with direct fast Fourier transform. EPSI captured the spatial distributions of both metabolites and their temporal dynamics in vivo with an in-plane spatial resolution of 5×9 mm^2 and a temporal resolution of 3 seconds. Significantly higher spatial and temporal resolution for delineating anatomical structures in vivo was achieved for EPSI metabolic maps than for CSI maps, which suffered spatiotemporal blurring. The EPSI sequence showed promising results in terms of short acquisition time and sufficient spectral bandwidth of 500 Hz, allowing to adjust the trade-off between signal-to-noise ratio and encoding speed.

INTRODUCTION

Since the introduction of the dissolution dynamic nuclear polarization (dDNP) technique (1), magnetic resonance spectroscopic of hyperpolarized ^{13}C has emerged as an attractive modality that enables imaging of metabolic activity in vivo (2–5). Currently, hyperpolarized ^{13}C metabolic imaging is being widely conducted in combination with the more established positron emission tomography (PET) (6, 7) to study its potential for clinical use. The hybrid PET/magnetic resonance imaging (MRI) systems are well suited for such tasks (8–10). The enhanced magnetization obtained from hyperpolarization methods is short-lived, and the magnetization consumed by excitations is nonrecoverable. This dictates the use of optimized imaging sequences that efficiently use the decaying magnetization. The conventional 2D phase-encoded chemical-shift imaging (CSI) sequence encodes the k-space using 2 phase-encoding gradients

ISSN 2379-1381 http://dx.doi.org/10.18383/j.tom.2018.00006

(11, 12). This results in a total imaging duration of CSI that is relatively long compared with the longitudinal relaxation time, and it gives poor resolution for mapping the dynamics of metabolism. Accelerated spectroscopic imaging sequences, such as echo-planar spectroscopic imaging (EPSI) (13–19), multiecho balanced steady-state free precession (ME-bSSFP) (20–22), spiral magnetic resonance spectroscopic imaging (MRSI) (23–26), and IDEAL spiral (27), require fewer excitations because >1 k-space position is sampled for each excitation, for example, 1 k-space line in the case of EPSI and ME-bSSFP and 1 image frame in the case of spiral acquisition. Therefore, the total imaging time for these sequences is reduced, typically by 1 order of magnitude. The short imaging time and fewer excitations make such sequences attractive for imaging of hyperpolarized nuclear spins, enabling observation of the conversion of the hyperpolarized substrates to their metabolic products with acceptable temporal resolution. These sequences, however, are characterized by a limited spectral bandwidth (SW) owing to gradient slew rate constraints. The dwell time (time elapsed between consecutive acquisitions of the same point in k-space) is governed by the gradient echo spacing in the case of ME-bSSFP (20–22) and EPSI (13–19), and the echo time (TE) increment between spirals in the case of spiral MRSI and IDEAL spiral (23–27). This reduced SW is usually not a limitation for hyperpolarized MRI, as the spectrum of the hyperpolarized ^{13}C substrate and its metabolic products is sparse, and spectral aliasing can be controlled to avoid peak overlap. However, compared with conventional CSI, these fast-acquisition sequences are more demanding in terms of gradient strength and slew rate, and they require extensive ramp sampling on clinical magnetic resonance (MR) scanners as opposed to preclinical systems, which reduces the signal-to-noise ratio (SNR) per unit time. These limitations of gradient performance make it challenging to translate the use of these sequences from small animals to human studies.

EPSI is the most established sequence to achieve dynamic imaging of the metabolism in clinical studies (28) with hyperpolarized pyruvate. This sequence uses oscillating gradients in the readout direction during data acquisition to efficiently sample 1 line at each repetition time (TR) interval at the expense of reduced SW. EPSI with symmetric readout gradients typically suffers from aliasing artifacts (29, 30) owing to gradient imperfection, which require reference scans to estimate and correct the discrepancies between the odd and even echoes (31). Flyback EPSI is sometimes preferred over symmetric EPSI to avoid the need to correct these differences (32, 33). However, flyback EPSI suffers from lower SNR because the receiver is idle for longer duration (16, 34). We argue that symmetric EPSI with separate reconstruction of the odd and even echo data is sufficient and simple, if the resultant smaller SW is acceptable. The simplest way to reconstruct the even and odd data is via fast Fourier transform (FFT) assuming that the data are collected on a Cartesian grid. However, the data in the k–t space are acquired on a zig-zag trajectory, so the phase evolution during the acquisition of individual k-space lines must be corrected before carrying out FFT to avoid spatial blurring due to chemical-shift artifacts in the opposite directions for odd-and-even gradient echoes.

In this study, we present symmetric ^{13}C EPSI with a separate reconstruction of the odd and even echo data and ramp sampling for application on a clinical PET/MRI system. An issue with hybrid PET/MR systems is that the performance of their gradients is lower than that of their nonhybrid counterparts. This makes the implementation of fast sequences more challenging. The EPSI technique is based on our proton EPSI methodology (35–38), which provides high sampling efficiency without ghosting and acceptable SW. Moreover, we apply a correction of the phase evolution during the acquisition of the zig-zag trajectory in the k–t space (39, 38), to avoid spatial blurring due to chemical-shift artifacts in the opposite directions for odd-and-even gradient echoes. This reconstruction algorithm is extended to give optimal reconstruction for sufficiently band-limited signals, even for aliased nonoverlapping peaks. Both free induction decay (FID) and spin-echo excitation methods were evaluated. The sequence was validated and compared with CSI by using a phantom with multiple compartments of ^{13}C-labeled compounds. Moreover, a version of the sequence with centric phase encoding was evaluated in vivo with hyperpolarized [1-^{13}C]pyruvate in a canine cancer patient undergoing PET/MR, as part of the diagnostic workup for acanthomatous ameloblastoma. This work is meant to be a feasibility study that paves the way for future large animal and human studies in which EPSI will be used. In one of our previous works (8–9), conventional CSI, which is not very suitable for dynamic or 3D imaging, was used. To the best of our knowledge, this is one of the first implementations of this sequence in a Siemens platform toward imaging hyperpolarized ^{13}C substrates.

METHODOLOGY

Hardware

All experiments were performed on a 3 T PET/MR (mMR Biograph, Siemens Healthcare, Erlangen, Germany), with a maximum gradient strength of 43 mT/m, a maximum slew rate of 180 mT/m/ms, a gradient raster time of 10 microseconds, an analog-to-digital converter (ADC) raster time of 100 nanoseconds, and a minimum delay between ADC readout events of 100 microseconds. The raster time is the smallest temporal unit that can be used to specify the timing of the ADC event. The acoustic resonances of the gradient coil were in the frequency bands of 530 – 630 Hz and 1010 – 1230 Hz. The system has a 2-kW transmit power.

Two coils were used in this work, a ^{13}C birdcage head coil (RAPID Biomedical, Rimpar, Germany) with a 265-mm inner diameter and a ^{1}H/^{13}C transmit/receive flex coil (RAPID Biomedical; 110-mm loop for ^{13}C and 180 × 244 mm butterfly for ^{1}H). The head coil was used with a thermal phantom, and the flex coil was used with a hyperpolarized [1-^{13}C]pyruvate phantom and in vivo with the canine cancer patient. A 7-mL vial with 4.0M ^{13}C-urea doped with gadolinium (0.23% v/v; Dotarem, Villepinte, Guerbet, France) was used for flip angle calibration in the hyperpolarized phantom experiment and in vivo. All stated flip angles are as calibrated at the position of the reference sample. Two phantoms were used. To compare the SNR between the sequences, a cylinder with a 250-mm diameter and 200-mm length was used. It had 4 cylindrical compartments with inner diameters of 19 mm each. The outer volume of the phantom was

filled with ethylene glycol with the natural abundance of ^{13}C, and 3 of the inner compartments were filled with ^{13}C-bicarbonate, [1-^{13}C]acetate, and ^{13}C-urea (all 3 compounds are from Sigma Aldrich, Brøndbyvester, Brøndby, Denmark). The concentration of each substrate is 1.0M. The 3 compounds were doped with Omniscan (GE Healthcare, Brøndby, Denmark) to T1 values of 0.4 seconds, 0.7 seconds, and 0.7 seconds (measured at 9.4 T and 295 K). The fourth compartment was left empty.

A hyperpolarized phantom made from a rectangular bottle ($200 \times 185 \times 125$ mm^3) was initially filled with 4.5-L of saline solution. A hyperpolarized sample containing 14 mmol of [1-^{13}C]pyruvate was added to the phantom after dissolution. Then the phantom was briefly shaken, placed on top of the surface ^{1}H/^{13}C coil, and dynamic imaging acquired. To prepare the hyperpolarized sample, 1 mL of [1-^{13}C]pyruvic acid with 15mM of electron paramagnetic agent, AH111501 (Syncom BV, Groningen, the Netherlands), was polarized in a SPINlab polarizer (GE Healthcare) for 4 h. The sample was then dissolved in 49.8 mL of dissolution media containing 0.1 g/L of EDTA (ethylenediaminetetraacetic acid disodium salt dehydrate; Sigma Aldrich) in water. The sample was neutralized with 14.6 mL of neutralizing media containing 0.72M NaOH, 0.4M 2-Amino-2-(hydroxymethyl)-1,3-propanediol (Sigma Aldrich) and 0.1 g/L EDTA disodium salt in water.

Design of ^{13}C EPSI

Echo Planar Readout Gradient. Both the desired spatial resolution and the target SW with separate processing of even and odd echo data (35, 36, 40) were taken into account when designing the trapezoidal echo planar readout gradient with ramp sampling. The echo spacing was chosen to avoid acoustic resonances, which must be outside of the ranges of 1.58–1.89 milliseconds and 810–990 microseconds. An SW of ~500 Hz in a 3 T magnet, which avoids acoustic resonances, is acceptable for the case of hyperpolarized [1-^{13}C]pyruvate. The pyruvate and its products alanine, pyruvate-hydrate, and lactate, are located at 171.1, 176.3, 177.6, and 183.2 ppm, respectively (i.e., a range of 372 Hz in a 3 T scanner).

The iterative design process for the targeted SW $= (2ES)^{-1}$ was initiated with a trapezoidal readout gradient waveform G_{RO} such that:

$$\Delta x = \frac{1}{\gamma \int_{t=0}^{t=T_{RO}} G_{RO}(t)dt} \qquad (1)$$

where Δx is the spatial resolution in the readout dimension, γ is the gyromagnetic ratio for the nucleus of interest, $t = 0$ is the start time of signal recording, T_{RO} is the readout time, and $T_{RO} < ES$. Further increase in spatial resolution requires increasing the readout time T_{RO} and thus reducing the SW.

An SW of ~500 Hz in a 3 T magnet is acceptable for the case of hyperpolarized [1-^{13}C]pyruvate. The pyruvate and its products alanine, pyruvate-hydrate, and lactate are located at 171.1, 176.3, 177.6, and 183.2 ppm, respectively (ie, a range of 372 Hz in a 3 T scanner).

The iterative optimization of the gradient waveform under the given hardware constraints yielded an SW of 495 Hz corresponding to a gradient lobe duration of 1010 microseconds. Using trapezoidal gradients with ramp-up and ramp-down durations of 170 microseconds, the maximum gradient strength achievable during ramping at the maximum slew rate was 30 mT/m. The ADC was switched on 57 microseconds after the start of the gradient and switched off 57 microseconds before the end of the gradient lobe to ensure >100 microseconds between successive ADC periods. The effective gradient moment accumulated during the readout was 26.6 mTs/m, which provided a maximum achievable spatial resolution of 3.75 mm with 495 Hz SW on the mMR Biograph. The corresponding ADC period was 896 microseconds.

If the reference frequency is chosen to be exactly in the middle between pyruvate and lactate, then the resultant spectrum acquired with a bandwidth of 495 Hz will be as shown in Figure 1A (lactate at 186 Hz, pyruvate-hydrate at 24 Hz, alanine at −21 Hz and pyruvate at −186 Hz). The bicarbonate signal will be aliased to the center of the spectrum at 1 Hz, between alanine and pyruvate-hydrate. The peak positions of the 3 substrates in the multicompartment phantom were acetate at 155 Hz, bicarbonate at 494 Hz (aliased to 71 Hz), and urea at 424 Hz (aliased to 1 Hz) (Figure 1B).

Phase-Encoding Gradient

The total duration of the phase-encoding gradient was set to 1700 microseconds giving a maximum resolution of 1.9 mm in the phase-encoding direction. An EPSI version with centric phase encoding was designed and used in the hyperpolarization experiments in phantom and in vivo.

Radiofrequency Pulses

An excitation pulse (Hanning-filtered sinc with a time bandwidth product of 4) with a total duration of 1280 microseconds and a central lobe duration of 640 microseconds was used. The smallest slice thickness achievable with this pulse was 6 mm, with a slice selection gradient of 43 mT/m. The excitation pulse used had an approximate bandwidth (BW) of 3000 Hz. The chemical shift displacement $\delta_{p,l}$ between pyruvate and lactate in the slice direction was, therefore:

$$\delta_{p,l} = \frac{\Delta f_{p,l}}{\gamma G_z} = \frac{\Delta f_{p,l}}{BW}\Delta z = 0.12\ \Delta z \qquad (2)$$

where $\Delta f_{p,l}$ is the chemical shift between pyruvate and lactate (372 Hz at 3 T) and Δz is the slice thickness.

In addition, a spin echo (SE) EPSI was implemented with Hanning-filtered sinc refocusing pulse with a time bandwidth product of 8. The duration of the refocusing pulse was set during the pulse preparation, and the smallest allowed duration is assumed (2600 microseconds) without exceeding the B1 limit. The maximum bandwidth of the pulse is therefore 2.2 kHz. The maximum allowable duration for the refocusing pulse was 7200 microseconds, giving a minimum bandwidth of 780 Hz. This sequence was used in the phantom SNR evaluation.

SNR Efficiency

We characterized the sensitivity of EPSI as a function of field strength and computed the ramp sampling efficiency as in the study by Otazo et al. (40). Pohmann et al. (41) compared different CSI methods and analyzed their sensitivity with respect to the conventional phase-encoded CSI. For an EPSI sequence, the sensitivity Ψ_{EPSI} can be related to the CSI sensitivity Ψ_{CSI} as follows:

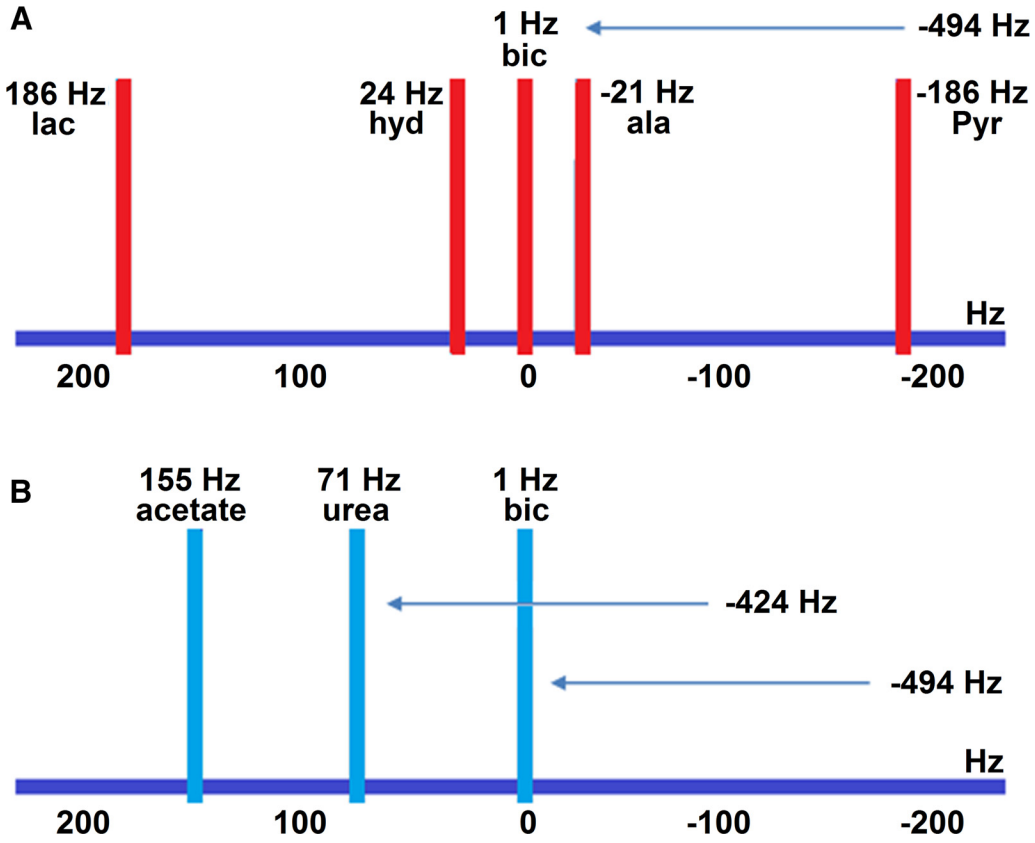

Figure 1. A diagram showing the peak positions of the metabolites with a SW of 495 Hz and a reference frequency chosen midway between lactate and pyruvate. After injection of hyperpolarized [1-^{13}C]pyruvate lactate appears at 186 Hz, pyruvate-hydrate at 24 Hz, alanine at –21 Hz, pyruvate at –186 Hz and bicarbonate aliased to 1 Hz (true position at –494 Hz) (A). The figure also shows the peak positions of the substrates used in the phantom experiment (B); acetate at 155 Hz and the aliased urea and bicarbonate at 71 Hz (true position, −424 Hz) and −1 Hz (true position, 494 Hz), respectively. In the phantom experiment, however, the actual reference frequency was chosen at the middle between bicarbonate and acetate to ensure uniform excitation for the substrates. These frequency positions were calculated based on a synthesizer frequency of 30.995 MHz, which corresponds to a magnetic field of 2.89 T. The chemical shift values in parts per million are obtained from: http://www.utsouthwestern.edu/education/medical-school/departments/airc/tools-references/chemical-shifts/chemical-shifts-sorted-by-compound-name.html.

$$\Omega_{EPSI} = \frac{\Psi_{EPSI}}{\Psi_{CSI}} = \sqrt{1 - \frac{\tau_s}{ES}} \qquad (4)$$

where τ_s is the time needed for gradient switching, and ES is the echo spacing.

Pipe and Duerk (42) showed that the variance in the reconstructed image depends on the shape of the gradient waveform used to record the signal. The smallest variance for even sampling occurs in the case of constant gradient, in which case, the variance in the reconstructed image is equal to the variance of the thermal noise σ^2. They also showed that the variance in the reconstructed image σ_i^2 can be expressed in terms of the first and second moments of the gradients waveform $G(t)$, the thermal noise variance σ^2, and the measurement duration T:

$$\frac{\sigma_i^2}{T} = \frac{\sigma^2 \int_0^T G^2(t)dt}{\left(\int_0^T G(T)dt\right)^2} \qquad (5)$$

Reconstruction and Postprocessing

Initially, 1D regridding was applied to compensate for uneven k-space sampling over the ramp. After regridding, the odd and even echoes were separated into 2 matrices. Time reversal was performed on the odd echo data. Temporal Fourier transformation was applied to the 2 data sets to obtain 2 k_x-k_y-f arrays. Before applying the spatial Fourier transform, a linear phase correction was introduced along the readout direction k_x (39, 38) to account for the time evolution, which would otherwise results in a chemical-shift displacement in the spatial domain, differing between even- and odd-numbered echoes. Subsequently, spatial Fourier transform was applied to obtain odd and even x-y-f matrices. The data corresponding to odd echoes were phase-adjusted and then added to the even echo data to obtain a ^{13}C spectroscopic image. The reconstructed spectra were interpolated to 256 points using zero-filling in the time domain. No apodization was used in the temporal dimension. Figure 2 shows the reconstruction pipeline. The chemical-shift correction de-

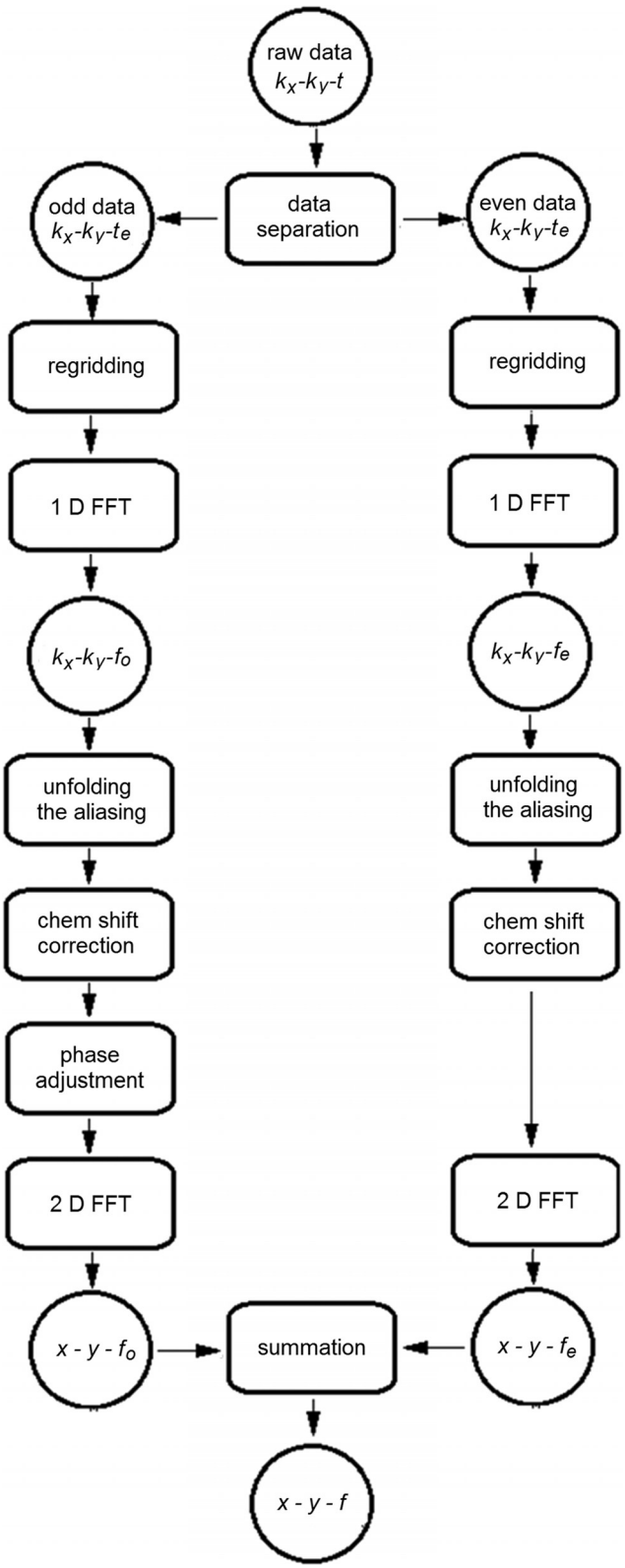

Figure 2. The pipeline used for the reconstruction of the raw data and the correction of the broadening due to chemical shifts in opposite directions for odd and even echoes.

scribed above assumes there is no aliasing of metabolites in the spectrum, which may occur in practice, as the SW is relatively small. Therefore, any aliased peaks should be unfolded to its true frequency position before applying the corrections. This can be done if peaks do not overlap in the aliased spectra by simply applying phase ramps corresponding to spatial shifts of nonaliased peak frequencies.

Phantom Experiment

An experiment was conducted to evaluate the SNR and the localization of the EPSI sequence using the birdcage coil and the multicompartment cylindrical phantom. A product CSI sequence served as the SNR reference. The CSI data were acquired with TR of 1,000 milliseconds, field of view (FOV) of 100 × 100 mm^2, spatial matrix of 16 × 16, flip angle of 90°, slice thickness of 100 mm, SW of 5000 Hz, number of spectral points of 512, sampling time of 102.4 milliseconds, and no averaging, resulting in a CSI scan time of 4 minutes and 16 seconds. The time between excitation and sampling was 2.3 milliseconds. EPSI data were acquired with a TR of 1000 milliseconds, an FOV of 100 × 100 mm^2, a spatial matrix of 16 × 16, a flip angle of 90°, a slice thickness of 100 mm, an echo train length of 128, an echo spacing of 1010 microseconds, and averages of 16, resulting in a scan time of 4 minutes and 16 seconds, an echo train duration of 129.3 milliseconds and an SW of 495 Hz. The time between excitation and start of the first readout gradient lobe was 2.4 milliseconds. In addition, SE-EPSI was acquired with the same parameters as EPSI, except TE was 8.8 milliseconds, i.e., the time to the first gradient echo. For noise estimation, both CSI and EPSI sequences were run after nulling the transmitted signal. These sequences were also evaluated using the 7-mL vial of ^{13}C-urea and the surface coil.

To quantify the SNR of each substrate, the signal was estimated at each voxel from the peak amplitude (real phased spectrum). Then the signal was averaged in a 4- × 4-pixel region of interest encompassing the substrate, and normalized by the noise standard deviation in the spectra in the same region of interest.

To assess the localization of the spectroscopic sequences, the proton image was taken as a reference. For each substrate, the location of the center of the cylinder in the ^{13}C image and in the proton image was compared. The shift in millimeters between the 2 locations was reported. Because each substrate is in a cylinder, a circle was fitted to the contour spatial distribution and the center of the circle was taken as the location in the proton image. The ^{13}C images were obtained using general linear model fitting. Then spline fitting was applied to the ^{13}C spatial distribution of each substrate to achieve subvoxel precision at the same resolution as the proton image. The position of the peak intensity in the metabolite distribution after spline fitting was used as the substrate location in the ^{13}C image.

A final phantom experiment was conducted with hyperpolarized [1-^{13}C]pyruvate and the surface coil. Two different dynamic measurements were acquired, one with EPSI and one with CSI. The EPSI acquisition was made using an FOV of 200 × 200 mm^2, a matrix of 32 × 32 with central phase encoding, an echo train length of 64, a flip angle of 6°, a TR of 80 milliseconds, and a TE of 2.4 milliseconds. The acquisition time per frame was 2.5 seconds and an image was acquired every 5 seconds. The CSI

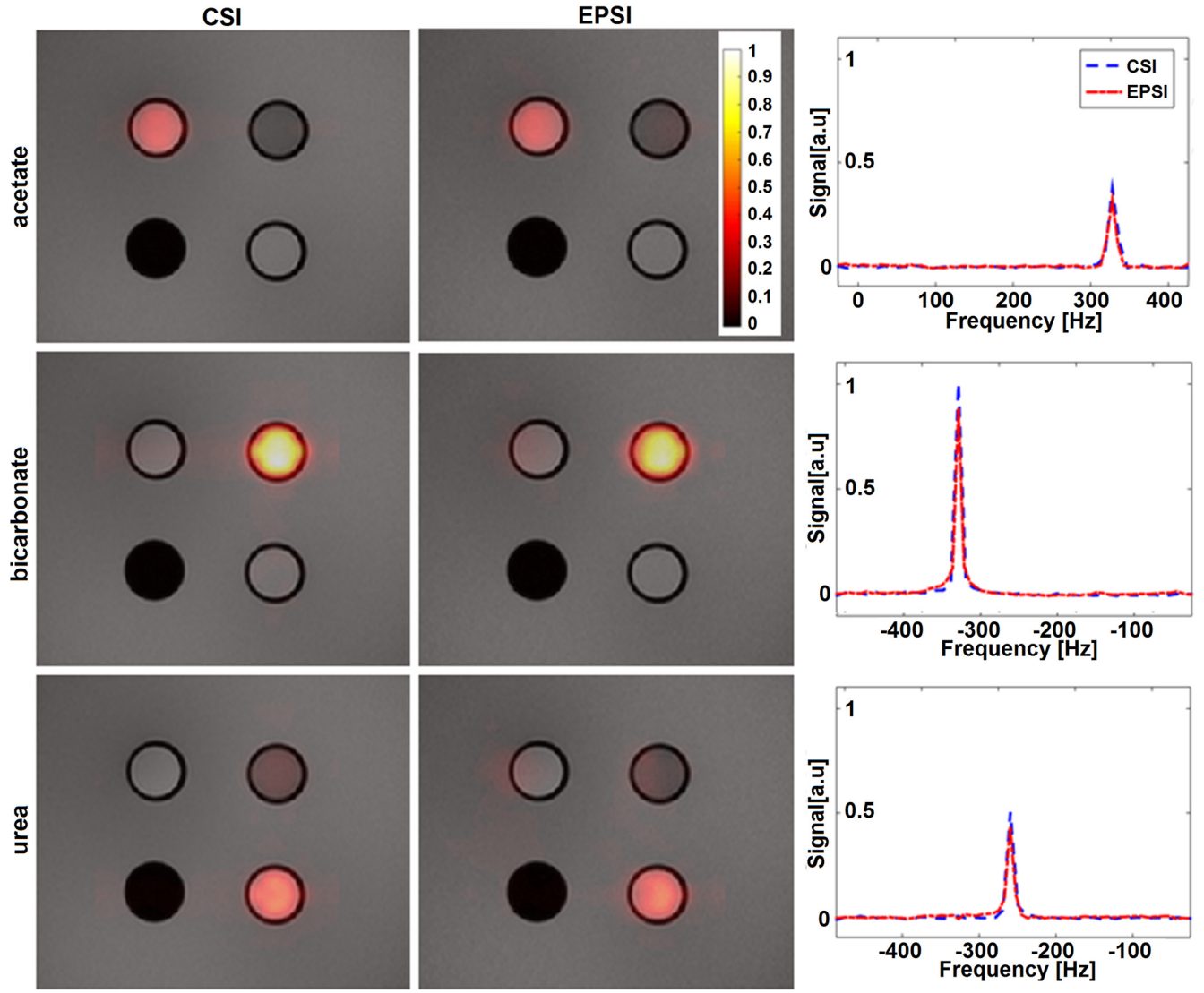

Figure 3. The [1-^{13}C]acetate, ^{13}C-bicarbonate, and ^{13}C-urea maps acquired by chemical-shift imaging (CSI) and echo-planar spectroscopic imaging (EPSI). Only the central part of the phantom is shown. The signal level in the maps is normalized with respect to the bicarbonate signal acquired with CSI. The spectrum from a single voxel at the center of each substrate is also shown for both CSI and EPSI. The line width (full width at half maximum) obtained with CSI was 12.2 Hz, 9.2 Hz, and 10.6 Hz for [1-^{13}C]acetate, ^{13}C-bicarbonate, and ^{13}C-urea, respectively, whereas the line width obtained with EPSI was 11.7 Hz, 8.7 Hz, and 9.8 Hz.

was acquired using an FOV of 200 × 200 mm^2, a truncated matrix of 16 × 16, a flip angle of 3°, a TR of 80 milliseconds, and a TE of 2.3 milliseconds. The acquisition time per frame was 12 seconds, and 3 images were acquired sequentially without delay.

Clinical Study in a Canine Cancer Patient With Ameloblastoma

A 9-year-old female intact Samojed dog weighing 27 kg with a histopathologically confirmed ameloblastoma of the left mandible underwent PET/MR examination as part of the diagnostic and staging workup prior to therapy. Hyperpolarized ^{13}C MRSI was included in this examination. The owner gave informed consent, and the study was approved by the Ethical and Administrative Committee, Department of Veterinary Clinical Sciences, Faculty of Health and Medical Sciences, University of Copenhagen.

Three 500-μL samples of [1-^{13}C]pyruvic acid with 15mM AH111501 were hyperpolarized in the SPINlab polarizer for 4 h. The samples were dissolved in 29.1 mL of dissolution media and neutralized with 7.3 mL of neutralizing media. After dissolution, 18 mL (0.68 mL/kg) of 250mM [1-^{13}C]pyruvate was injected intravenously over 7–8 seconds.

Coronal, transversal, and sagittal anatomic ^{1}H MR images were acquired for planning using a T2-weighted turbo SE sequence (TR, 4,000 milliseconds; TE, 89 milliseconds; voxel size, 0.5 × 0.5 mm^2; slice, 19; thickness, 3 mm).

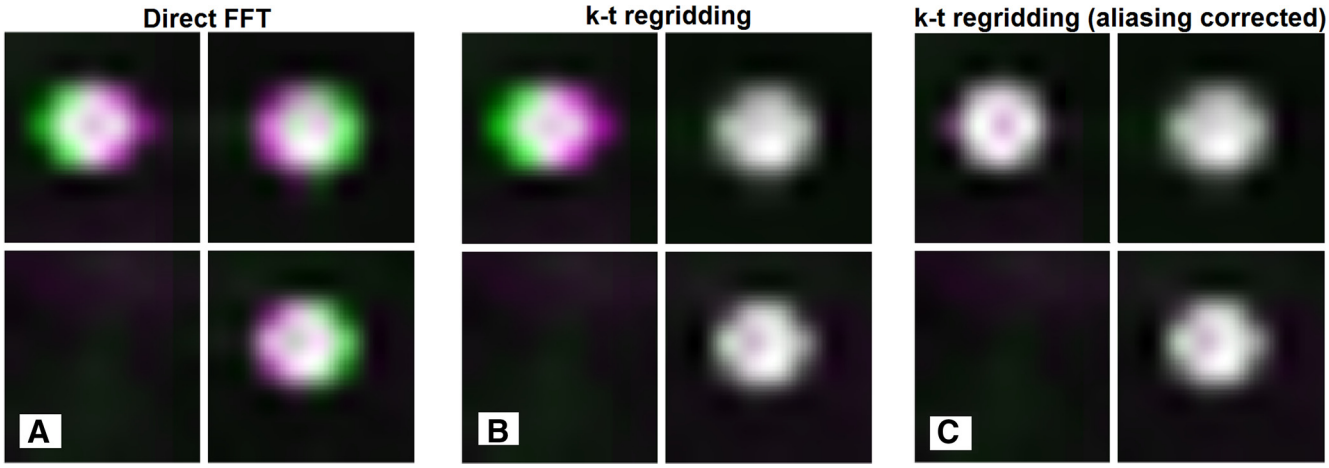

Figure 4. A comparison of chemical-shift displacement with direct fast Fourier transform (FFT) reconstruction (A) and reconstruction after spectral-spatial regridding (B and C). The images from odd (green) and even (magenta) echoes are overlaid. The locations of the overlap appear in white and those of the nonoverlap appear colored. In (B), spectral-spatial regridding removes the chemical-shift displacement of bicarbonate and urea, which are within the SW, but increases the chemical-shift displacement of acetate that is aliased. In (C), the chemical-shift displacement of the acetate peak is additionally corrected using its nonaliased frequency location in the reconstruction.

The dog received 3 injections of hyperpolarized [1-^{13}C]pyruvate in 10-minute intervals. A dynamic FID sequence with no in-plane spatial encoding was started at the beginning of the sample injection with the following parameters: slice thickness, 4 cm; TR, 1 second; flip angle, 5°; acquisition delay, 2.3 milliseconds; SW, 6000 Hz; and points, 512. The purpose of the dynamic FID was to find the time point with maximum lactate signal, which was used to determine the start time of the subsequent CSI acquisition. Acquisition of a CSI data set was initiated 30 seconds after the start of the injection of the second pyruvate sample with a TR of 80 ms, an FOV of 150 × 180 mm^2, a matrix size of 16 × 16, slice thickness of 15 mm, a flip angle of 10°, an acquisition delay of 2.3 milliseconds, an SW of 10 000 Hz, and number of spectral points of 512. A dynamic EPSI acquisition was started at the end of the injection of the third hyperpolarized sample using an FOV of 150 × 180 mm^2, a matrix central phase encoding of 16 × 32, a slice thickness of 15 mm, an echo train length of 64, a flip angle of 6°, a TR of 80 milliseconds, and an acquisition delay of 2.4 milliseconds. The acquisition time per frame was 1.3 seconds and a frame was acquired every 3 seconds (with an idle time of 1.7 seconds between frames).

PET images were acquired as a single bed with a 5-minute acquisition duration, after intravenous injection of 216 MBq (8 MBq/kg) of ^{18}F-2-fluoro-2-deoxy-D-glucose (^{18}F-FDG) 1 hour before imaging. PET reconstruction used ordinary Poisson 3D ordered subset expectation maximization with 4 iterations, 21 subsets, 344 × 344 matrix, 4-mm 3D Gaussian postfilter, 2.1- × 2.1-mm^2 pixel size, and 2.0-mm slice thickness.

RESULTS

Phantom Experiments

To calculate the theoretical relative SNR between the CSI and the EPSI, Eq. (4) was used. The EPSI acquisition time was 896 microseconds with 114-microsecond delay between acquisitions reducing the SNR by 5% compared with CSI. To account for ramp sampling, Eq. (5) was used to calculate the SNR efficiency relative to a square readout gradient waveform, which amounts to 94%. Therefore, the relative theoretical SNR of EPSI with respect to CSI was 89%.

Figure 3 shows the signal for the 3 substrates, namely, ^{13}C-urea, ^{13}C-bicarbonate, and [1-^{13}C]acetate in the multicompartment phantom obtained with CSI and EPSI using the birdcage coil, superimposed on the proton image. The strength of the signal varied between the substrates owing to differences in T1 relaxation time constants and line width. The SNR measurements from the multicompartment phantom were repeated twice. In the first phantom experiment, the SNR measured was as follows: for the CSI, the SNR values were 290, 153, and 113 for ^{13}C-bicarbonate, ^{13}C-urea, and [1-^{13}C]acetate, respectively. For EPSI, the SNR values were 257, 135, and 99 for the 3 phantoms ^{13}C-bicarbonate, ^{13}C-urea, and [1-^{13}C]acetate, respectively. The SNR values for SE EPSI were 170, 86, and 67 for ^{13}C-bicarbonate, ^{13}C-urea, and [1-^{13}C]acetate, respectively. In the second phantom experiment, the CSI SNR values were 257, 128, and 141. The measured SNR values for FID EPSI were 220, 115, and 121, whereas SE EPSI had SNR values of 162, 90, and 82 for the 3 metabolites. Thus, the calculated relative SNR values of FID EPSI with respect to CSI were 0.87 ± 0.02, 0.89 ± 0.01, and 0.86 ± 0.01 for ^{13}C-bicarbonate, ^{13}C-urea, and [1-^{13}C]acetate, respectively, whereas the relative SNR values of SE EPSI were 0.61 ± 0.03, 0.63 ± 0.09, and 0.59 ± 0.01 for the 3 metabolites. The CSI had the smallest spatial offsets with a discrepancy of 0.8 mm for [1-^{13}C]acetate, 0.9 mm for ^{13}C-bicarbonate, and 1.5 mm for ^{13}C-urea. The offsets were larger for the EPSI sequence: 1.9 mm, 1.7 mm, and 3.1 mm for ^{13}C-bicarbonate, ^{13}C-urea, and [1-^{13}C]acetate, respectively.

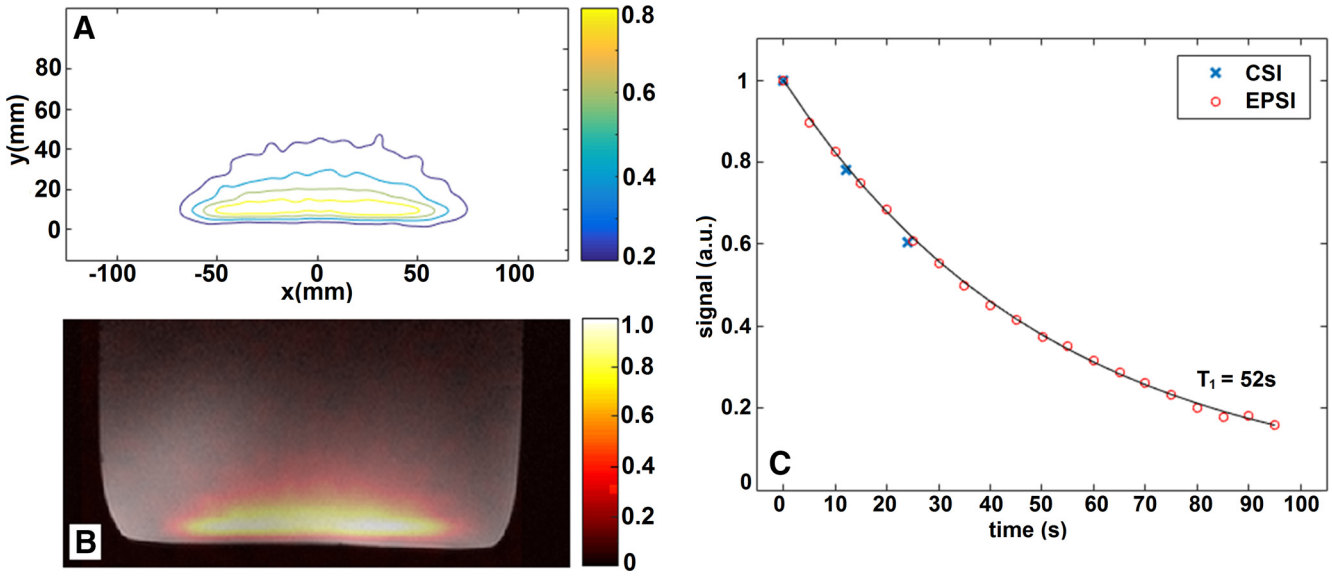

Figure 5. The first dynamic image acquired for hyperpolarized [1-^{13}C]pyruvate in a 4.5-L phantom with EPSI in (B) and the coil profile (A). The normalized coil profile was derived from the EPSI image of the phantom and is proportional to B1^2. Decay of the signal from hyperpolarized pyruvate obtained by both EPSI and CSI dynamics (C). An exponential function was fitted to the EPSI signal giving a time constant of 52 seconds.

The SNR values obtained with the ^{13}C-urea vial and the surface coil were 283 for CSI, 245 for EPSI, and 263 for SE EPSI. This corresponds to relative SNR values of 0.87 and 0.93 for EPSI and SE EPSI with respect to CSI, respectively.

Figure 4 shows the comparison between EPSI reconstruction algorithms. Direct FFT reconstruction (Figure 4A) results in spatial blurring of the substrates in the ^{13}C image owing to chemical shifts in opposite directions for even and odd echoes. On the other hand, spectral-spatial regridding using the apparent frequency positions (Figure 4B) results in a narrower and more accurate spatial representation of ^{13}C-urea and ^{13}C-bicarbonate. [1-^{13}C]Acetate, however, was outside of the critically sampled bandwidth, and therefore aliased, which resulted in increased spatial broadening. When accounting for aliasing by using the actual frequency offset of the nonaliased peak when calculating phase ramps, the chemical-shift displacement of [1-^{13}C]acetate was compensated as well (Figure 4C). The dynamic signal acquired for hyperpolarized [1-^{13}C]pyruvate in the 4.5-L rectangular phantom (sum of the signal over the phantom) with both CSI and EPSI is shown in Figure 5C. For the dynamic measurements obtained with CSI (see Figure 5), the time resolution was very coarse, 12 seconds, despite the smaller matrix size used, and thus, had coarser spatial resolution. The coil profile derived from the EPSI image of the phantom is shown in Figure 5A.

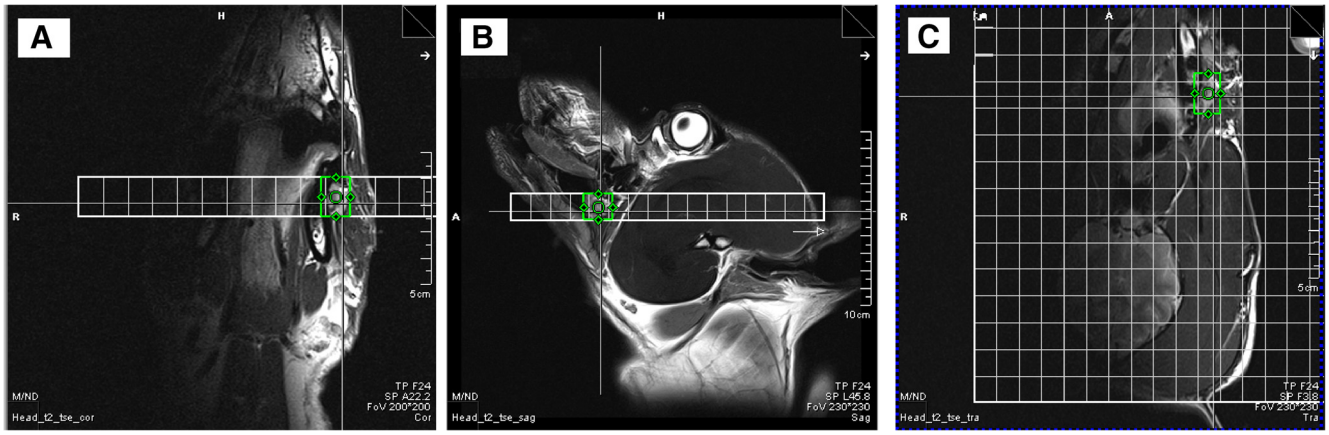

Figure 6. The anatomical images (transversal, coronal, and sagittal) acquired with turbo spin echo and used to position the spectroscopic grids for both CSI and EPSI (A, B, and C). The green box is at the location of the tumor.

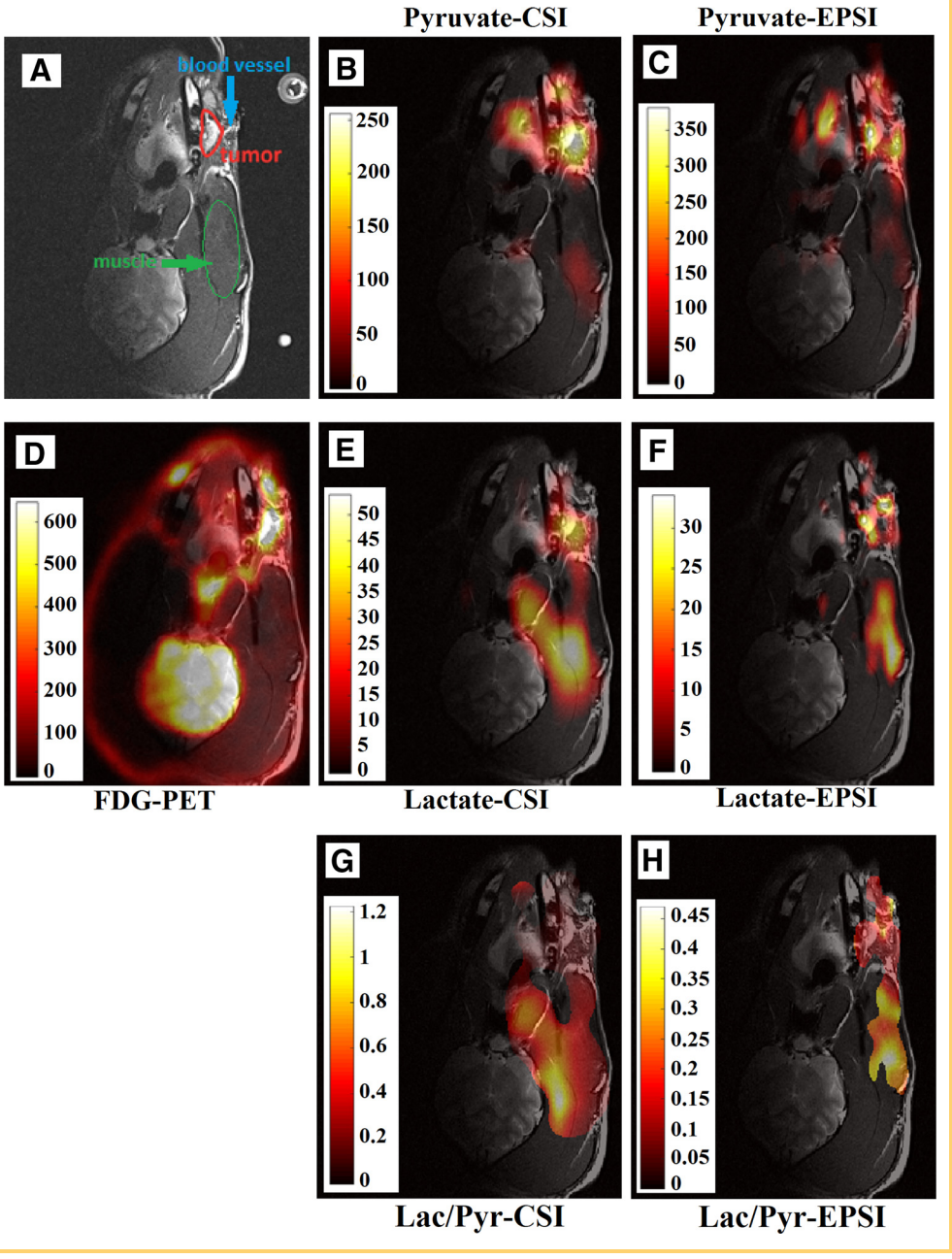

Figure 7. The acanthomatous ameloblastoma in the left mandible of the canine (A). Positron emission tomography-fludeoxyglucose (PET-FDG) image (slice thickness, 2 mm) with high uptake in the tumor and brain regions (D). The pyruvate and lactate signals from the CSI acquisition in the slice containing the tumor, calculated using general linear model (GLM) analysis (B and C). Increased lactate production can be observed at the tumor and muscle sites. Pyruvate and lactate images calculated from the dynamic EPSI by integrating over the frames in Figure 9 (C and F). Lactate to pyruvate ratios obtained from CSI and EPSI (G and H).

Canine PET/Hyperpolarized MR Evaluation

Figure 6 shows the anatomical images used to plan the positioning of the spectroscopic grids for both CSI and EPSI. The 16- × 12-mm tumor is located at the buccal side of the left mandible (as shown in Figure 7A). The dynamic FID (Figure 8A) shows that pyruvate starts accumulating in the slab containing the tumor about 10 seconds after the start of the injection, and it reaches peak value 9 seconds later. The lactate starts building up 22 seconds after the start of the injection and reaches a maximum value after 32 seconds. The CSI acquisition was timed to start 30 seconds after injection to obtain the highest possible lactate signal from the slice. Figure 7, B and E shows the pyruvate and lactate signals at the slice containing the tumor. Relatively high pyruvate uptake and an increased lactate production can be observed at the tumor site. In addition, lactate signal can be seen at the masticator muscle in the lower right region. The PET-FDG image (Figure 7D) also shows high metabolism at the tumor site in addition to the typical high FDG uptake in the brain.

In Figure 9, the series of metabolic maps obtained with EPSI are given. These maps show the buildup and decay of pyruvate and lactate across the slice. To allow for comparison with the dynamic FID, the pyruvate and lactate signals in each frame were summed over the entire frame, to obtain the time plots shown in Figure 8B. The pyruvate and lactate signals were also integrated at the tumor and masticator muscles to obtain dynamic buildup and decay at these 2 sites (Figure 8, C and D). Moreover, the pyruvate and lactate series were integrated into 1 pyruvate and 1 lactate image (Figure 7, C and F) for comparison with the corresponding CSI maps in Figure 7, B and E. The signal level in all the metabolic maps

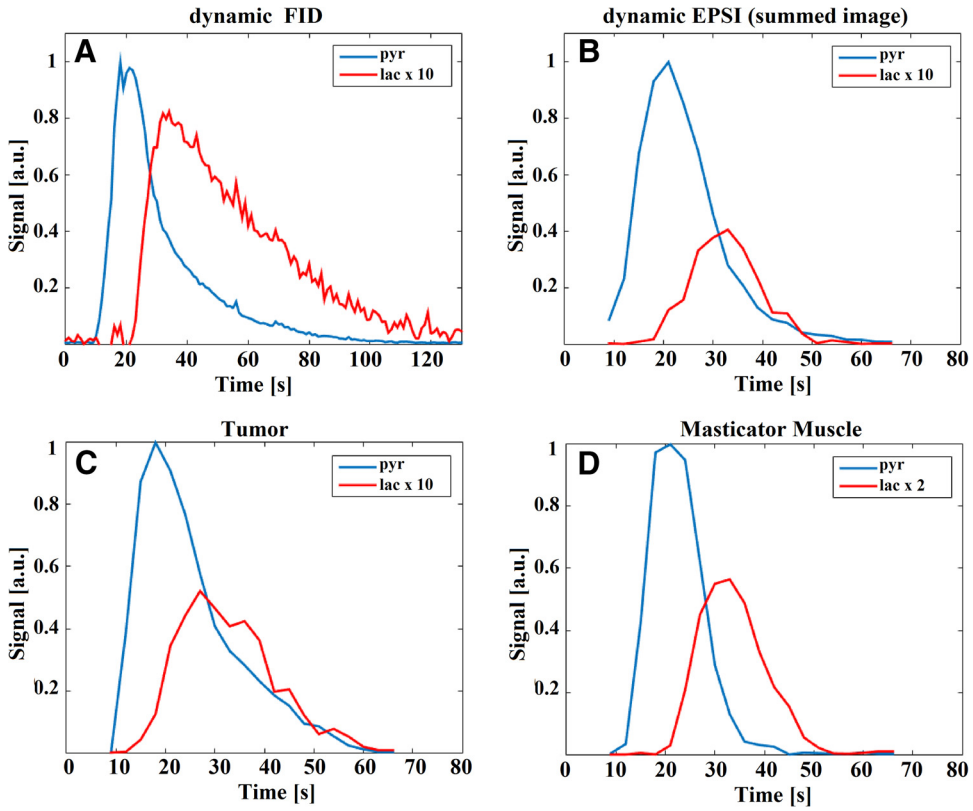

Figure 8. The buildup of pyruvate and its conversion to lactate obtained with dynamic free induction decay (FID) acquisition over a 4-cm axial slab that includes the tumor region (A). Time curves for lactate and pyruvate obtained from the EPSI series (Figure 9) by integrating the pyruvate and lactate signals in each frame over the whole image, over the tumor region, and over the masticator muscle (B–D).

in Figures 7 and 8 was normalized with respect to the standard deviation of the noise.

DISCUSSION

This work presents an implementation of a symmetric EPSI sequence for hyperpolarized ^{13}C in a hybrid clinical PET/MR system. The reconstruction pipeline uses a phase correction to combine odd and even echoes that enables adequate SW and spatial and temporal resolution for hyperpolarized metabolic imaging of [1-^{13}C]pyruvate. The implementation is demonstrated in phantoms and in vivo. The EPSI SNR was around 87% compared with CSI, and this agrees with the theoretical estimation and literature (33).

Although EPSI is susceptible to errors from gradient waveform imperfection, these errors were minor in this work. However, higher resolution can increase the demand on gradients, and this in turn could increase artifacts with this sequence. This may explain the error in localization in which the substrates were slightly shifted outward. However, on average, the localization error was less than one-third of the voxel dimension, and the estimate may also be influenced by noise. Although all the substrates in the multicompartment phantom had the same concentration, the SNR as measured from the CSI and EPSI acquisitions varied significantly owing to the differences in T1 relaxation times.

With the birdcage coil, the SNR of the SE EPSI was ~61% of the CSI SNR, in contrast to 93% with the surface coil. This discrepancy in SNR values of SE EPSI is because of the difference in the refocusing pulse durations used with the 2 coils. Because of the relatively high power needed with the birdcage coil, the bandwidth of the refocusing pulse was limited to ~1000 Hz. This range is sufficient for the pyruvate–lactate range, but insufficient to uniformly cover the range from bicarbonate to acetate in the phantom experiments (peak separation, 650 Hz). SE EPSI has not been used in vivo owing to B1 inhomogeneity, as we were using surface coil and the pulses implemented were nonadiabatic. The SE EPSI, however, will be improved further to suit in vivo imaging and thus allow us to make use of the relatively long T2 of hyperpolarized substrates.

The reconstruction used in this work provides better accuracy compared with direct FFT. For EPSI with flyback readout (33), direct FFT will cause few artifacts, as the chemical shift displacement is in 1 direction and no broadening occurs. Aliased metabolites caused an error in the spatial-spectral regridding. This error was removed by adapting the algorithm to exploit that the ^{13}C spectrum in the hyperpolarization experiments is sparse and the metabolite frequencies known *a priori*. Other examples of hyperpolarized ^{13}C substrates that give sparse spectra, with 2 or 3 peaks, and for which this EPSI sequence can be used without major modifications include, but is not limited to, hyperpolarized ^{13}C-bicarbonate used to measure pH values (34) and [1,4-^{13}C]fumarate used in imaging necrosis (44).

In a previous work (16) that also used EPSI, the gradient amplitude used was considerably smaller than the maximum limit owing to the relatively low bandwidth used, and therefore, the effect of eddy currents was insignificant. This allowed full bandwidth reconstruction without Nyquist ghosting. In another study by the same group (17), a similar approach to the one described in our work was used. In that work, the odd and even data were reconstructed separately and their magnitudes were summed to form the final spectra. However, neither phase

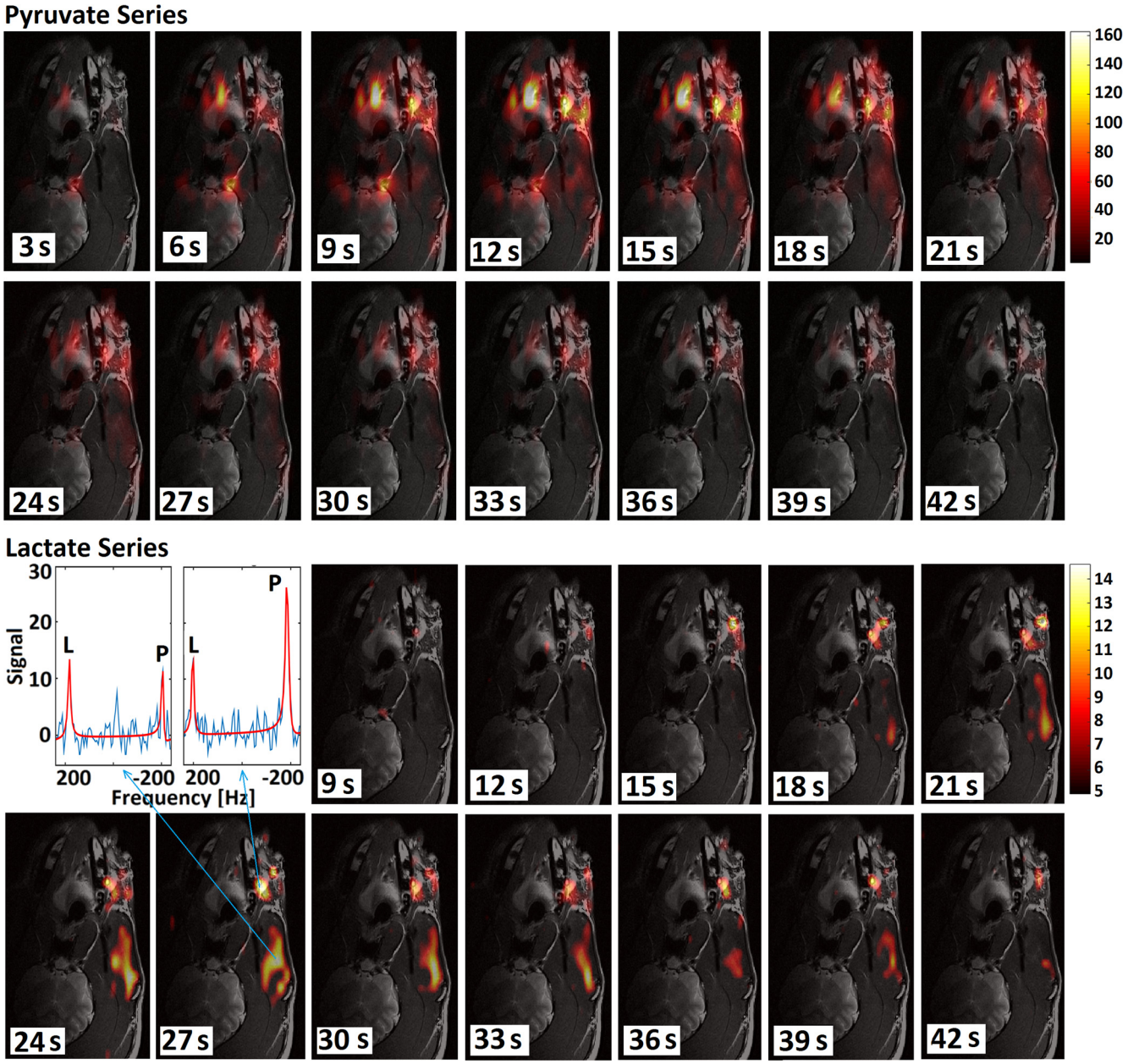

Figure 9. Pyruvate and lactate buildup and decay across the slice containing the tumor. The figure also shows an example spectrum with GLM fitting at the tumor site in the EPSI frame acquired 27 seconds after the end of injection.

matching between odd and even data nor chemical shift correction was used.

In the phantom experiment with hyperpolarized [1-^{13}C]pyruvate, EPSI allowed dynamic imaging with reasonable temporal resolution. However, faster imaging could have been achieved using fewer phase-encoding steps, as the surface coil had a relatively superficial localized sensitivity, and most of the signals came from a small part of the FOV. Similarly, for the in vivo evaluation in the canine, most of the observed signals came from the jaw close to the surface coil, where the tumor was located.

Higher spatial resolution was achieved for the metabolic maps obtained with EPSI compared with CSI in the hyperpolarization experiments. Despite using dynamic acquisition with EPSI in the in vivo hyperpolarization experiment, using a larger matrix size was feasible, compared with the matrix size of CSI. Moreover, CSI is prone to blurring from T1 decay owing to the relatively long acquisition duration per frame. Therefore, the pyruvate and lactate signals were sharper and better localized in the EPSI metabolic maps, whereas the maps obtained from the CSI acquisition were blurry. The blurring due to T1 decay can be mitigated by using variable flip angle scheme to uniformly distribute the decaying magnetization over the acquisition window.

The dynamic measurements of pyruvate and lactate in Figure 8B obtained from EPSI agree with those obtained from

the dynamic FID sequence (Figure 8A). Lactate reached the maximum about 27 seconds after the end of the injection (34 seconds after the start) in the EPSI series, whereas pyruvate was highest 13 seconds after the end of injection (20 seconds from the start of injection). The maximum lactate signal relative to maximum pyruvate was higher for the dynamic FID sequence compared with EPSI. This is probably because of the higher number of excitations per unit time in the EPSI sequence that consumes more pyruvate magnetization before the conversion to lactate (5.3 excitations per s with 6° flip angle reduces the signal by 2.9%/s compared with the 5° flip angle every second for the FID giving 0.4%/s signal reduction). Both the EPSI and the CSI sequences showed similar metabolite distributions. The slight differences could be because the imaging windows for the 2 sequences were different: CSI was acquired over 12 seconds from 30 seconds after injection, whereas EPSI was acquired over 60 seconds from the end of the injection. Also, the spatial resolution of CSI was lower than that of EPSI. The 2 sequences also used different excitation profiles over time as explained above.

No detectable signal was observed from bicarbonate in this experiment. The surface coil was relatively away from the brain region. Imaging bicarbonate can be challenging owing to its relatively low SNR and short T2. Spectral selective pulses or multiband excitation can optimize the use of the hyperpolarized magnetization and have a better chance at detecting bicarbonate.

In conclusion, an implementation of a symmetric EPSI sequence in a clinical PET/MR system was presented with an adopted reconstruction that provides more accurate spatial mapping of the hyperpolarized signal compared with direct FFT, also for aliased nonoverlapping peaks. EPSI provided an acceptable trade-off between encoding speed and SNR in the phantom and in vivo experiments. Moreover, the in vivo experiment showed that the designed sequence provides high temporal and spatial resolution for mapping hyperpolarized metabolites and their dynamic behavior.

ACKNOWLEDGMENTS

The Mind Research Network is acknowledged for providing their facilities to conduct the initial experiments. We would also like to acknowledge the financial support from Danish Research Council (Grant Number 1331-00259A), the Danish National Research Foundation (Grant Number DNRF124), and Innovation Fund Denmark.

Disclosures: No disclosures to report.

Conflict of Interest: The authors have no conflict of interest to declare.

REFERENCES

1. Ardenkjaer-Larsen JH, Fridlund B, Gram A, Hansson G, Hansson L, Lerche MH, Servin R, Thaning M, Golman K. Increase in signal-to-noise ratio of > 10,000 times in liquid-state NMR. Proc Natl Acad Sci U S A. 2003;100:10158–10163.
2. Golman K, Zandt RI, Lerche M, Pehrson R, Ardenkjaer-Larsen JH. Metabolic imaging by hyperpolarized 13C magnetic resonance imaging for in vivo tumor diagnosis. Cancer Res. 2006;66:10855–10860.
3. Day SE, Kettunen MI, Gallagher FA, Hu D-E, Lerche MH, Wolber J, Golman K, Ardenkjaer-Larsen JH, Brindle KM. Detecting tumor response to treatment using hyperpolarized 13C magnetic resonance imaging and spectroscopy. Nat Med. 2007;13:1382–1387.
4. Albers MJ, Bok R, Chen AP, Cunningham CH, Zierhut ML, Zhang VY, Kohler SJ, Tropp J, Hurd RE, Yen YF, Nelson SJ, Vigneron DB, Kurhanewicz J. Hyperpolarized 13C lactate, pyruvate, and alanine: Noninvasive biomarkers for prostate cancer detection and grading. Cancer Res. 2008;68:8607–8615.
5. Kurhanewicz J, Vigneron DB, Brindle K, Chekmenev EY, Comment A, Cunningham CH, Deberardinis RJ, Green GG, Leach MO, Rajan SS, Rizi RR, Ross BD, Warren WS, Malloy CR. Analysis of cancer metabolism by imaging hyperpolarized nuclei: prospects for translation to clinical research. Neoplasia. 2011;13:81–97.
6. Gallagher FA, Bohndiek SE, Kettunen MI, Lewis DY, Soloviev D, Brindle KM. Hyperpolarized 13C MRI and PET: in vivo tumor biochemistry. J Nucl Med. 2011; 52:1333–1336.
7. Torigian DA, Kjær A, Zaidi H, Alavi A. PET/MR imaging: clinical applications. PET Clin. 2016;11:10–12.
8. Gutte H, Hansen AE, Henriksen ST, Johannesen HH, Ardenkjaer-Larsen JH, Vignaud A, Hansen AE, Børresen B, Klausen TL, Wittekind A-MN, Gillings N, Kristensen AT, Clemmensen A, Højgaard L, Kjær A. Simultaneous hyperpolarized 13C-pyruvate MRI and 18F-FDG-PET in cancer (hyperPET): feasibility of a new imaging concept using a clinical PET/MRI scanner. Am J Nucl Med Mol Imaging. 2015;5:38–45.
9. Gutte H, Hansen AE, Larsen MME, Rahbek S, Henriksen ST, Johannesen HH, Ardenkjaer-Larsen JH, Kristensen AT, Højgaard L, Kjær A. Simultaneous hyperpolarized 13C-pyruvate MRI and 18F-FDG PET (hyperPET) in 10 dogs with cancer. J Nucl Med. 2015;56:1786–1792.
10. Hansen AE, Andersen FL, Henriksen ST, Vignaud A, Ardenkjaer-Larsen JH, Højgaard L, Kjaer A, Klausen TL. Simultaneous PET/MRI with 13 C magnetic resonance spectroscopic imaging (hyperPET): phantom-based evaluation of PET quantification. EJNMMI Phys. 2016;3:7–20.
11. Brown TR, Kincaid BM, Ugurbil K. NMR chemical shift imaging in three dimensions. Proc Natl Acad Sci U S A. 1982;79:3523–3526.
12. Maudsley AA, Hilal SK, Perman WH, Simon HE. Spatially resolved high resolution spectroscopy by "four-dimensional" NMR. J Magn Reson. 1983;51:147–152.
13. Cunningham CH, Vigneron DB, Chen AP, Xu D, Nelson SJ, Hurd RE, Kelley DA, Pauly JM. Design of flyback echo-planar readout gradients for magnetic resonance spectroscopic imaging. Magn Reson Med. 2005;54:1286–1289.
14. Cunningham CH, Chen AP, Albers MJ, Kurhanewicz J, Hurd RE, Yen YF, Pauly JM, Nelson SJ, Vigneron DB. Double spin-echo sequence for rapid spectroscopic imaging of hyperpolarized 13C. J Magn Reson. 2007;187:357–362.
15. Larson PEZ, Kerr AB, Chen AP, Lustig MS, Zierhut ML, Hu S, Cunningham CH, Pauly JM, Kurhanewicz J, Vigneron DB. Multiband excitation pulses for hyperpolarized 13C dynamic chemical-shift imaging. J Magn Reson. 2008;194:121–127.
16. Yen YF, Kohler SJ, Chen AP, Tropp J, Bok R, Wolber J, Albers MJ, Gram KA, Zierhut ML, Park I, Zhang V, Hu S, Nelson SJ, Vigneron DB, Kurhanewicz J, Dirven HAAM, Hurd RE. Imaging considerations for in vivo 13C metabolic mapping using hyperpolarized 13C-pyruvate. Magn Reson Med. 2009;62:1–10.
17. Larson PEZ, Bok R, Kerr AB, Lustig M, Hu S, Chen AP, Nelson SJ, Pauly JM, Kurhanewicz J, Vigneron DB. Investigation of tumor hyperpolarized [1-13C]-pyruvate dynamics using time-resolved multiband RF excitation echo-planar MRSI. Magn Reson Med. 2010;63:582–591.
18. Larson PE, Hu S, Lustig M, Kerr AB, Nelson SJ, Kurhanewicz J, Pauly JM, Vigneron DB. Fast dynamic 3D MR spectroscopic imaging with compressed sensing and multiband excitation pulses for hyperpolarized 13C studies. Magn Reson Med. 2011;65:610–619.
19. Tropp J, Lupo JM, Chen A, Calderon P, McCune D, Grafendorfer T, Ozturk-Isik E, Larson PE, Hu S, Yen YF, Robb F, Bok R, Schulte R, Xu D, Hurd R, Vigneron D, Nelson S. Multi-channel metabolic imaging, with SENSE reconstruction, of hyperpolarized [1-13C] pyruvate in a live rat at 3.0 tesla on a clinical MR scanner. J Magn Reson. 2011;208:171–177.
20. Leupold J, Wieben O, Månsson S, Speck O, Scheffler K, Petersson JS, Hennig J. Fast chemical shift mapping with multiecho balanced SSFP. MAGMA. 2006;19: 267–273.
21. Leupold J, Månsson S, Stefan Petersson J, Hennig J, Wieben O. Fast multiecho balanced SSFP metabolite mapping of 1H and hyperpolarized 13C compounds. MAGMA. 2009;22:251–256.
22. Perman WH, Bhattacharya P, Leupold J, Lin AP, Harris KC, Norton VA, Hovener JB, Ross BD. Fast volumetric spatial-spectral MR imaging of hyperpolarized 13C-labeled compounds using multiple echo 3D bSSFP. Magn Reson Imaging. 2010; 28:459–465.

23. Josan S, Yen YF, Hurd R, Pfefferbaum A, Spielman D, Mayer D. Application of double spin echo spiral chemical shift imaging to rapid metabolic mapping of hyperpolarized [1-13C]-pyruvate. J Magn Reson. 2011;209:332–336.
24. Josan S, Hurd R, Park JM, Yen YF, Watkins R, Pfefferbaum A, Spielman D, Mayer D. Dynamic metabolic imaging of hyperpolarized [2-13C]pyruvate using spiral chemical shift imaging with alternating spectral band excitation. Magn Reson Med. 2014;71:2051–2058.
25. Park JM, Josan S, Jang T, Merchant M, Watkins R, Hurd RE, Recht LD, Mayer D, Spielman DM. Volumetric spiral chemical shift imaging of hyperpolarized [2-13C]pyruvate in a rat c6 glioma model. Magn Reson Med. 2016;75:973–984.
26. Mayer D, Yen YF, Levin YS, Tropp J, Pfefferbaum A, Hurd RE, Spielman DM. In vivo application of sub-second spiral chemical shift imaging (CSI) to hyperpolarized 13C metabolic imaging: Comparison with phase-encoded CSI. J Magn Reson. 2010;204:340–345.
27. Wiesinger F, Weidl E, Menzel MI, Janich MA, Khegai O, Glaser SJ, Haase A, Schwaiger M, Schulte RF. IDEAL spiral CSI for dynamic metabolic MR imaging of hyperpolarized [1-13C]pyruvate. Magn Reson Med. 2012;68:8–16.
28. Nelson SJ, Kurhanewicz J, Vigneron DB, Larson PE, Harzstark AL, Ferrone M, van Criekinge M, Chang JW, Bok R, Park I, Reed G, Carvajal L, Small EJ, Munster P, Weinberg VK, Ardenkjaer-Larsen JH, Chen AP, Hurd RE, Odegardstuen LI, Robb FJ, Tropp J, Murray JA. Metabolic imaging of patients with prostate cancer using hyperpolarized [1-^{13}C]pyruvate. Sci Transl Med. 2013;5:198ra108.
29. Bruder H, Fischer H, Reinfelder HE, Schmitt F. Image reconstruction for echo planar imaging with nonequidistant k-space sampling. Magn Reson Med. 1992;23:311–323.
30. Du YP, Zhou XJ, Bernstein MA. Correction of concomitant magnetic field-induced image artifacts in nonaxial echo-planar imaging. Magn Reson Med. 2002;48:509–515.
31. Gordon JW, Vigneron DB, Larson PE. Development of a symmetric echo planar imaging framework for clinical translation of rapid dynamic hyperpolarized 13C imaging. Magn Reson Med. 2017;77:826–832.
32. Lupo JM, Chen AP, Zierhut ML, Bok RA, Cunningham CH, Kurhanewicz J, Vigneron DB, Nelson SJ. Analysis of hyperpolarized dynamic 13C lactate imaging in a transgenic mouse model of prostate cancer. Magn Reson Imaging. 2010;28:153–162.
33. Durst M, Koellisch U, Frank A, Rancan G, Gringeri CV, Karas V, Wiesinger F, Menzel MI, Schwaiger M, Haase A, Schulte RF. Comparison of acquisition schemes for hyperpolarised 13C imaging. NMR Biomed. 2015;28:715–725.
34. Jiang W, Lustig M, Larson PE. Concentric rings K-space trajectory for hyperpolarized 13C MR spectroscopic imaging. Magn Reson Med. 2016;75:19–31.
35. Posse S, DeCarli C, Le Bihan D. Three-dimensional echo-planar MR spectroscopic imaging at short echo times in the human brain. Radiology. 1994;192:733–738.
36. Posse S, Tedeschi G, Risinger R, Ogg R, Le Bihan D. High speed 1H spectroscopic imaging in human brain by echo planar spatial-spectral encoding. Magn Reson Med. 1995;33:34–40.
37. Posse S, Otazo R, Caprihan A, Bustillo J, Chen H, Henry PG, Marjanska M, Gasparovic C, Zuo C, Magnotta V, Mueller B, Mullins P, Renshaw P, Ugurbil K, Lim KO, Alger JR. Proton echo-planar spectroscopic imaging of J-coupled resonances in human brain at 3 and 4 Tesla. Magn Reson Med. 2007;58:236–244.
38. Hanson LG, Schaumburg K, Paulson OB. Reconstruction strategy for echo planar spectroscopy and its application to partially undersampled imaging. Magn Reson Med. 2000;44:412–417.
39. Metzger G, Hu X. Application of interlaced Fourier transform to echo-planar spectroscopic imaging. J Magn Reson. 1997;125:166–170.
40. Otazo R, Mueller B, Ugurbil K, Wald L, Posse S. Signal-to-noise ratio and spectral linewidth improvements between 1.5 and 7 Tesla in proton echo-planar spectroscopic imaging. Magn Reson Med. 2006;56:1200–1210.
41. Pohmann R, von Kienlin M, Haase A. Theoretical evaluation and comparison of fast chemical shift imaging methods. J Magn Reson. 1997;129:145–160.
42. Pipe J, Duerk JL. Analytical resolution and noise characteristics of linearly reconstructed magnetic resonance data with arbitrary k-space sampling. Magn Reson Med. 1995;34:170–178.
43. Gallagher FA, Kettunen MI, Day SE, Hu DE, Ardenkjær-Larsen JH, Jensen PR, Karlsson M, Golman K, Lerche MH, Brindle KM. Magnetic resonance imaging of pH in vivo using hyperpolarized 13C-labelled bicarbonate. Nature. 2008;453:940–943.
44. Gallagher FA, Kettunen MI, Hu DE, Jensen PR, Karlsson M, Gisselsson A, Nelson SK, Witney TH, Bohndiek SE, Hansson G, Peitersen T, Lerche MH, Brindle KM. Production of hyperpolarized [1, 4-13C2] malate from [1, 4-13C2] fumarate is a marker of cell necrosis and treatment response in tumors. Proc Natl Acad Sci U S A. 2009;106:19801–19806.